

Check for updates

Unraveling the Orientation-Property Relationship in Graphene Fibers for Enhanced Microwave Absorption

He Hao, Zheng Wang, Tianze Liu, Lianming Tong, * Xin Gao, * and Jin Zhang *

Graphene fibers hold great promise for next-generation microwave absorption (MA) applications, but their performance is often hindered by poor impedance matching and inefficient electromagnetic wave attenuation. In this study, it is demonstrated that graphene orientation is a critical structural parameter for optimizing MA performance. By utilizing expansion-extension flows during coaxial wet spinning, precise tuning of graphene orientation from axial to radial alignment is achieved. A real-time polarized optical characterization platform enables operando monitoring of orientation evolution, revealing a predictable relationship between flow parameters and graphene alignment. Experimental measurements and electromagnetic simulations show that the orientation of graphene fibers governs internal electric field distribution and impedance matching, resulting in a tunable MA response. Optimized fibers exhibit an effective absorption bandwidth of 6.28 GHz and a minimum reflection loss of -66.7 dB. These findings position orientation engineering as a powerful strategy for enhancing MA materials and provide a generalizable framework for structure-property optimization in macroscopic nanocarbon assemblies.

1. Introduction

Low-dimension nanocarbon materials such as graphene and carbon nanotubes (CNTs) are promising candidates for microwave

H. Hao, J. Zhang

Beijing Science and Engineering Center for Nanocarbons Beijing National Laboratory for Molecular Sciences

College of Chemistry and Molecular Engineering

Peking University Beijing 100871, China

E-mail: jinzhang@pku.edu.cn

Z. Wang, X. Gao, J. Zhang

School of Materials Science and Engineering

Peking University Beijing 100871, China

E-mail: gaoxin-cnc@pku.edu.cn

T. Liu, L. Tong

School of Advanced Materials

Peking University Shenzhen Graduate School

Shenzhen, Guangdong 518055, China

E-mail: tonglm@pku.edu.cn

X. Gao, J. Zhang

Beijing Graphene Institute (BGI)

Beijing 100095, China

The ORCID identification number(s) for the author(s) of this article can be found under https://doi.org/10.1002/adfm.202519036

DOI: 10.1002/adfm.202519036

absorption (MA) applications, owing to their tunable electrical properties, low density, and chemical durability.[1-6] Assembling these materials into fibers enables the translation of their exceptional intrinsic properties into macroscopic, flexible, and lightweight formats suitable for MA devices.[7-14] However. their performance is often limited by poor impedance matching and insufficient energy dissipation mechanisms.[15]

To address these limitations, prior efforts have focused on incorporating magnetic nanoparticles[8-13] or designing porous architectures^[7,8,13] to enhance magnetic loss and multiple scattering. Yet, these approaches frequently encounter challenges such as particle agglomeration, environmental instability[15], and fabrication complexity.[16] A more fundamental, but underexplored strategy, involves manipulating the orientation of anisotropic nanocarbons during fiber formation.

Graphene and CNTs exhibit intrinsically anisotropic electrical and electromagnetic responses.[2-4,17,18] Controlled alignment within fibers offers a powerful means to tailor electromagnetic wave propagation and attenuation. While orientation engineering has demonstrated promise in bulk aerogels, [19-21] its potential in fiber systems remains largely untapped due to the lack of methods for wide-range orientation control and real-time, quantitative tracking of orientation evolution during fabrication.

Existing orientation modulation techniques for fibers primarily focus on aligning nanocarbons either along the fiber axis via shear stress during stretching,[22-27] or radially through expansion flow in microfluidic devices. [28] However, these methods offer only limited control, tuning orientations within narrow angular ranges close to axial or radial directions. This restricts the exploration of the relationship between orientation and MA performance. For orientation characterization, polarized optical microscopy (POM) provides only qualitative insights based on brightness or interference colors [29-31] while cross-sectional scanning electron microscopy (SEM)[28,32-34] and small-angle Xray diffraction (SAXS)[30] allow quantitative but static or lowtemporal-resolution analysis. The need for fiber post-treatment (SEM) and low temporal resolution (SAXS) limits their use in operando studies of rapid orientation evolution, which are essential for understanding and controlling fiber formation processes. Therefore, the development of methods enabling both wide-range orientation fine-tuning and operando, quantitative

1616328.8, D. Downloaded from https://advanced.onlinelibrary.wiley.com/doi/10.1002/adfm.20219036 by Peking University Health, Wiley Online Library on p23/102025]. See the Terms and Conditions (https://onlinelibrary.vivey.com/ems-and-conditions) on Wiley Online Library for rules of use; OA articles are governed by the applicable Ceative Commons Is

Figure 1. Orientation fine-tuning, *operando* characterization, and orientation-property relationship for fibers. Short line segments in the orientation distribution images indicate local orientation directions. Black pixels can be regarded as the background region (see details in Note S3, Supporting Information). Abbreviations: GO, graphene oxide; Alg, alginate; OB, objective; DM, dichroic mirror; BS, beam splitter; LP, linear polarizer; HC, high-speed camera.

· Operando characterization

orientation tracking is critical to fully realize the potential of orientation engineering for optimizing nanocarbon fiber-based MA performance.

Orientation fine-tuning

Here, we report a coaxial wet-spinning strategy that enables continuous, tunable alignment of graphene sheets from axial to radial orientations, mediated by an expansion-extension flow field. Using operando simultaneous polarimetry, we track the dynamic orientation evolution in real time and introduce a semiellipsoid shell model that quantitatively links nanomaterial orientation to flow field parameters. This framework enables predictive tuning of orientation distributions during spinning. MA measurements reveal a strong orientation dependence: optimized fibers achieve an effective absorption bandwidth (EAB) of 6.28 GHz and a minimum reflection loss (RL) of -66.7 dB. Electromagnetic simulations indicate that radially aligned (vertical) fibers offer superior impedance matching and energy attenuation due to enhanced field penetration into the fiber core. Our findings establish orientation engineering as a critical design strategy for nanocarbon fibers and provide both fabrication and characterization tools to harness this control. Beyond MA applications, this platform may also enable advances in energy storage, [33,34] thermal regulation,[32] and artificial actuators,[35] where directional control of charge, heat, or strain is essential.

2. Results and Discussion

2.1. Integrated Platform for Graphene Orientation Control and Real-Time Characterization in Fibers

To fabricate fibers with tunable graphene sheet orientation, we developed a coaxial wet-spinning method that integrates the core/shell flow interfacial self-adaption strategy^[36] with mechanical drawing.^[31] As shown in **Figure 1**, graphene oxide (GO)

and sodium alginate (Alg) aqueous solutions were used as the core and shell fluid, respectively, and co-ejected into a calcium chloride ($CaCl_2$) coagulation bath via a coaxial spinneret (Figure S1a,b, Supporting Information). Mechanical drawing was applied using a take-up roller with a controllable linear velocity ($v_{\rm draw}$).

· Orientation-property relationship

At the spinneret outlet, the initial flow speeds of GO (v_{GO}) and Alg (v_{Alg}) were set to 90.76 and 12.17 mm s⁻¹, respectively. At low v_{draw}, the slower-moving Alg shell exerts a restriction effect that causes spontaneous equalization of v_{GO} and v_{Alg} , leading to deceleration of the GO core flow.[36] As the volume flow rate of the GO solution remains constant, this deceleration induces expansion of the GO core cross-section, generating an expansion flow.[28,29] Under this condition, GO sheets tend to align perpendicular to the fiber axis (Figure S1c, Supporting Information). As v_{draw} increases, the mechanical drawing imposes an extension effect that gradually overcomes the hydrogel deformation induced by v_{GO}-v_{Alg} equalization (Figure S1d, Supporting Information). At sufficiently high v_{draw}, an extension-dominated flow regime is established, [31] in which the GO sheets preferentially align parallel to the fiber axis (Figure S1e, Supporting Information).

To validate the proposed mechanism of GO orientation manipulation, we developed a four-channel division-of-amplitude simultaneous polarimetric system to monitor the dynamic evolution of GO alignment during coaxial wet-spinning (Figure 1; Figure S2a, Supporting Information). In this setup, the fiber was illuminated by unpolarized monochromatic light (wavelength = 550 nm). The transmitted light was collected by an objective lens and equally split into four optical paths without changing polarization states. Each path passed through a linear polarizer with a specific transmitting axis orientation before being focused onto a high-speed camera, producing four polarization-resolved

16163028, 0, Downloaded

onlinelibrary. wiley. com/doi/10.1002/adfm.202519036 by Peking University Health, Wiley Online Library on [23/10/2025]. See the Terms and Conditions (https://onlinelibrary.wiley.

conditions) on Wiley Online Library for rules of use; OA articles are governed by the applicable Creative Commons I

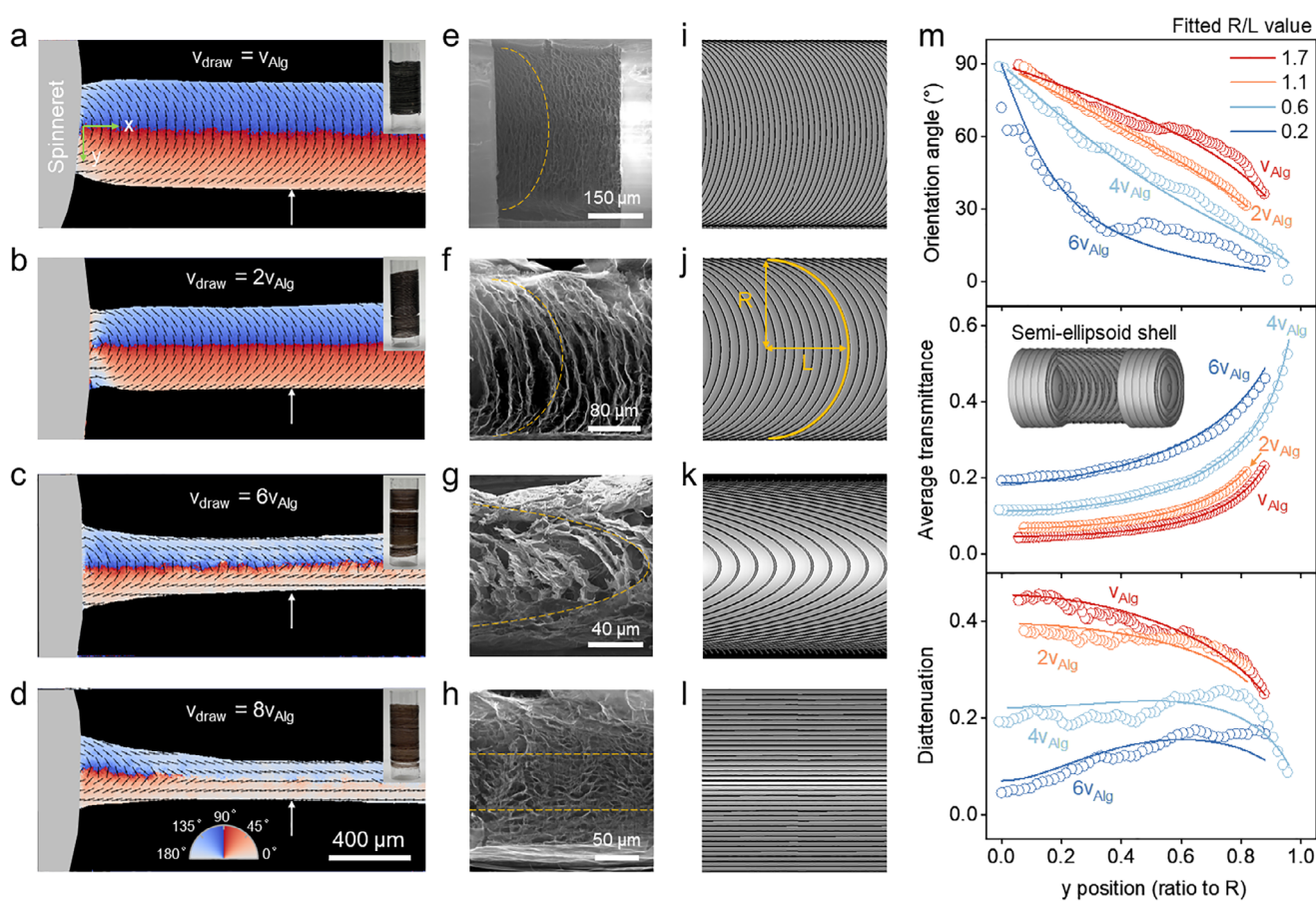


Figure 2. Operando characterization and unified description of GO orientation distribution in fibers. a–d) Operando orientation distribution images of GO/Alg fibers spun at drawing speeds of v_{Alg} (a), $2v_{Alg}$ (b), $6v_{Alg}$ (c), and $8v_{Alg}$ (d). Short line segments indicate local orientation directions. Black pixels can be considered as background regions (see details in Note S3, Supporting Information). The spinneret is shown in gray. Insets in (a-d) show photographs of the corresponding GO/Alg fibers wound on a 9-cm-long bobbin. e–h) Corresponding xy-plane cross-sectional SEM images of the fibers in a-d after freeze-drying. Orange dashed lines serve as visual guides highlighting sequential semi-ellipsoid shell-like structures. i–l) Simulated xy-plane cross-sectional structures matching the SEM images in (e–h). R, fiber radius; L, long axis length of the semi-ellipsoid shell. m) Local orientation, average transmittance, and diattenuation distribution extracted from the regions marked with white arrows in (a–d) and Figure S7a (Supporting Information). Solid lines represent fitting curves based on the semi-ellipsoid shell model. Experiment data (hollow circles) are extracted from Figure 2a–d, Figures S5f–o and S7 (Supporting Information) using the method described in Figure S7 (Supporting Information).

images in a single exposure (Figure S2b, Supporting Information). Leveraging the intrinsic diattenuation characteristics of GO, we extracted the local orientation angle (θ), average transmittance (T_{ave}), and diattenuation (D) at each pixel using Jones matrix calculation from the transmitted light intensity (Note S1, Supporting Information). The resulting orientation distribution map is shown in the top right corner of Figure 1, with corresponding average transmittance and diattenuation data presented in Figure S2c,d (Supporting Information).

The high temporal resolution of the imaging system allows real-time tracking of rapid GO orientation changes during the spinning process, providing quantitative insight into the evolving flow field. The orientation angle measurement error of the system is within $\pm 2^{\circ}$ (Figure S3, Supporting Information). Furthermore, a control experiment on pure Alg fibers confirmed that the Alg shell layer has a negligible impact on the accurate determination of GO orientation (Figure S4, Supporting Information), validating the reliability of our characterization method.

2.2. Expansion-Extension Flows Mediated GO Orientation Fine-Tuning

Using the simultaneous polarimetric system described above, we first performed *operando* observations of fiber structural evolution near the spinneret (**Figure 2**a–d; Figures S5 and S7, and Videos S1–s5, Supporting Information). As v_{draw} increased from v_{Alg} to $8v_{Alg}$, we observed a progressive transition in GO sheet orientation. The vertically aligned region near the fiber core gradually diminished, while the parallel alignment near the fiber shell expanded and eventually dominated the entire fiber at $v_{draw} = 8v_{Alg}$. Cross-sectional SEM images of the corresponding freezedried aerogel fibers exhibited consistent trends (Figure 2e–h; Figure S7c, Supporting Information), confirming the successful fabrication of GO fibers with a broad range of orientation distributions. These results validate the wade-range orientation control capability of our coaxial wet-spinning approach.

To further understand the mechanism of orientation finetuning, we developed a 3D semi-ellipsoid shell model to

16163028, 0, Downloaded from https

linelibrary.wiley.com/doi/10.1002/adfm.202519036 by Peking University Health, Wiley Online Library on [23/10/2025]. See the Terms and Conditions (https://onlinelibrary.wiley

conditions) on Wiley Online Library for rules of use; OA articles are governed by the applicable Creative Commons I

www.afm-journal.de

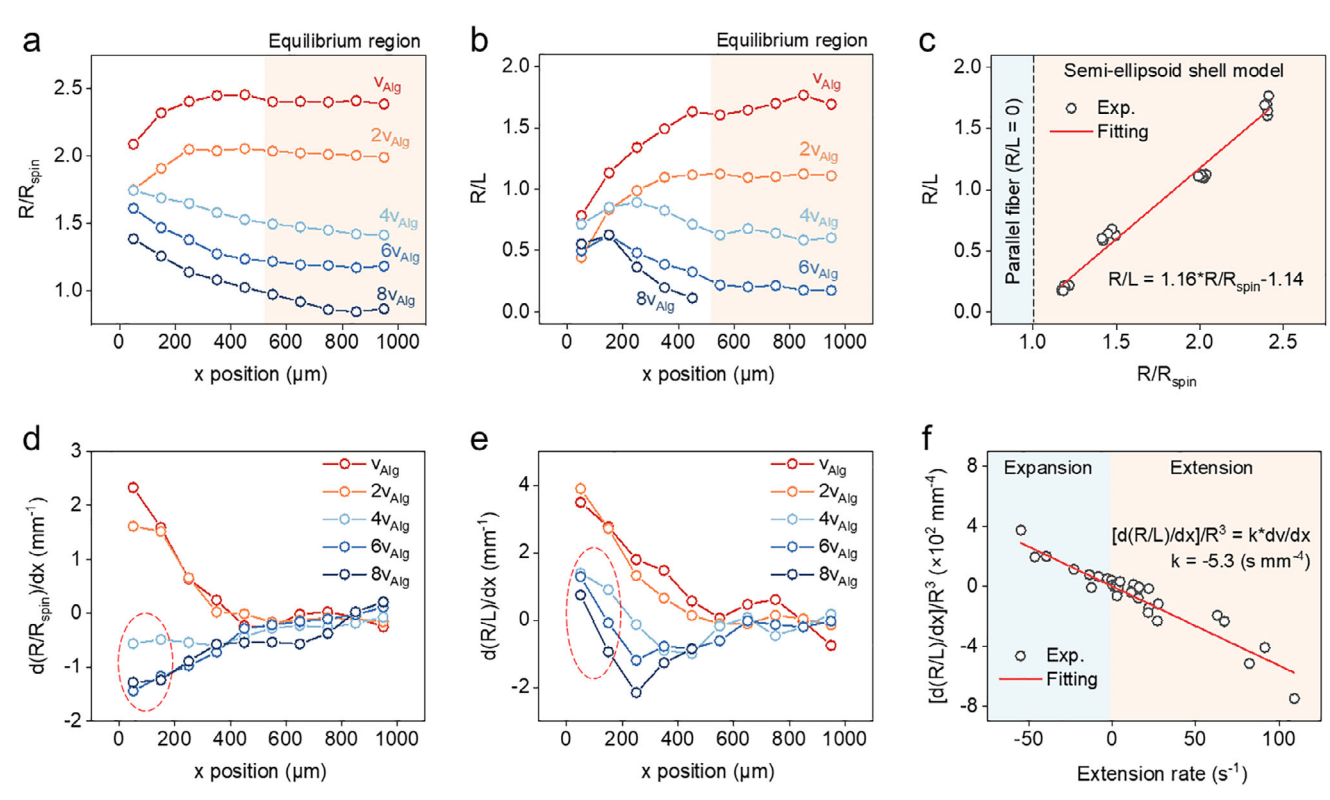


Figure 3. Quantitative analysis of the GO orientation evolution mechanism in fibers. a, b) Evolution of R/R_{spin} (a) and R/L (b) along the x-direction for different fibers. c) Relationship between R/R_{spin} and R/L in the equilibrium region of (a,b). $R_{spin} = 125 \mu m$ denotes the inner radius of the spinneret inner needle. The red solid line represents a linear fit to the experiment data, with a coefficient of determination (R-Square) of 0.982. d, e) Derivatives $d(R/R_{spin})/dx$ (d) and d(R/L)/dx (e) along the x-direction for different fibers. Data points within the red dashed circles are excluded from the analysis in Figure 3f due to complex counteraction between expansion and extension flows (see details in Note S5, Supporting Information). f) Relationship between $[d(R/L)/dx]/R^3$ and extension rate. The red solid line is a linear fit to the experimental data, yielding an R-Square of 0.903.

reconstruct the GO sheet orientation from the 2D polarimetry data (Figure S6 and Note S2, Supporting Information). For fibers spun at $v_{draw} \le 6v_{Alg}$, both polarimetry (Figure 2a–c) and SEM images (Figure 2e-g) revealed a radial variation in orientation, with GO sheets transitioning from perpendicular (90°) at the fiber center to nearly parallel (0°) at the fiber surface. This variation forms a series of parallel semi-ellipsoidal shells of aligned GO sheets (Figure 2i-k, inset of Figure 2m, and orange dashed lines in Figure 2e-g). Assuming rotational symmetry about the fiber axis, each GO sheet can be considered tangential to one of these shells (Figure S6b, Supporting Information). In this model, the complex 3D orientation distribution of GO is parameterized by the ratio of the fiber radius (R) to the semi-ellipsoid's long axis length (L) (Figure 2j). Given that polarimetry operates in transmission mode, the orientation maps in Figure 2a-d can be viewed as 2D projections of the 3D structure onto the xy-plane. This allows us to extract the R/L ratio retrospectively from the polarimetry data (Figures S6–S13, Notes S2 and S3, and Table S1, Supporting Information). Figure 2m shows both the experimentally measured and theoretically fitted θ , T_{ave} and D profiles along the y-axis at $x = 950 \mu m$ (marked by white arrows in Figure 2a-d). Using the extracted R/L values, we reconstructed theoretical cross-sections (Figure 2i-l) that closely match the experimentally observed orientation results (Figure 2e-h). To streamline this process, we further developed a simplified

2D semi-ellipse shell model (Figure S14, Supporting Information) that allows rapid extraction of R/L values directly from θ distribution data alone (Note S4, Figures S16–S20, Supporting Information).

Leveraging the combination of simultaneous polarimetry and semi-ellipsoid shell model, we quantitatively analyzed the GO orientation distribution in fibers and its correlation with flow behavior during wet spinning. Figure 3a,b summarizes the extracted values of fiber radius normalized to the spinneret inner radius (R/R_{spin}) and the R/L values for different samples (see Figures S9–S13, S15–S19, Supporting Information). To focus on stable fiber structures, we analyzed the "equilibrium region" where both fiber radius and GO orientation become consistent along the fiber axis (indicated in Figure 3a,b). From this region, we extracted the R/R_{spin} and R/L values, as shown in Figure 3c. Interestingly, for cases where R/R_{spin} \geq 1, the data points from fibers spun at different drawing speeds cluster along a nearly linear trend. This linear relationship can be expressed as:

$$R/L = 1.16R/R_{spin} + 1.14 (1)$$

This phenomenon indicates the following conclusions: 1) There is a positive linear correlation between $R/R_{\rm spin}$ and R/L. In previous works, $R/R_{\rm spin}$ is used as an indicator for the degree of flow expansion during the fiber spinning process, [28,29] but its

www.afm-journal.de

16163028, 0, Downloaded from https://advanced.onlineltbrary.wiley.com/doi/10.1002/affm.202519036 by Peking University Health, Wiley Online Library on [23/10/2025]. See the Terms and Conditions (https://onlinelibrary.wiley.com/emrs-and-conditions) on Wiley Online Library for rules of use; 0A article are governed by the applicable Creative Commons Library on [23/10/2025]. See the Terms and Conditions (https://onlinelibrary.wiley.com/emrs-and-conditions) on Wiley Online Library for rules of use; 0A article are governed by the applicable Creative Commons Library (https://onlinelibrary.wiley.com/emrs-and-conditions) on Wiley Online Library for rules of use; 0A article are governed by the applicable Creative Commons Library (https://onlinelibrary.wiley.com/emrs-and-conditions) on Wiley Online Library for rules of use; 0A article are governed by the applicable Creative Commons Library (https://onlinelibrary.wiley.com/emrs-and-conditions) on Wiley Online Library for rules of use; 0A article are governed by the applicable Creative Commons Library (https://onlinelibrary.wiley.com/emrs-and-conditions) on Wiley Online Library (https://onlinelibrary.wiley.com/emrs-and-conditions) on

relationship with nanomaterial orientation distribution remains unclear. Here, we quantitatively demonstrated that a larger degree of flow expansion is beneficial to acquiring a fiber with a higher R/L value and a larger vertically oriented region. 2) As R approaches R_{spin}, R/L converges toward zero. In this regime, L becomes much greater than R, and the semi-ellipsoid shell model degenerates into a "multiwalled concentric tubes" model, in which nanomaterials predominantly align along the fiber axis (Figure 21). This observation suggests that fibers with $R/R_{spin} \le$ 1 are likely to exhibit parallel alignment (Figure 2d,h,l), whereas $R/R_{spin} > 1$ is a necessary condition to form a vertically aligned region. Together, these results indicate that R/R_{spin} serves as a simple and robust structural indicator for predicting the orientation distribution in wet-spun nanocarbon fibers.

Having established a fundamental understanding of the final equilibrium fiber structures, we next investigated the orientation evolution behavior during the wet-spinning process. In prior studies, it has been shown that the stress applied to the fiber is the primary driving force for microscopic orientation evolution.[31] The ratio between shear rate $(\dot{\gamma})$ and expansion rate $(\dot{\varepsilon})$ governs the resulting nanomaterial orientation structure, with a critical threshold of $\dot{\varepsilon}/|\dot{\gamma}| > 0.14$ required to achieve vertical alignment of nanosheets relative to the flow direction. [30] However, this theory relies on a simplified model, assuming a sharp transition between either parallel or perpendicular alignment relative to the fiber axis, thereby neglecting intermediate or spatially varying orientation states. In contrast, our work incorporates a more realistic representation using the semi-ellipsoid shell model, which accounts for the full spectrum of 3D nanomaterial orientations within the fiber cross-section.

To this end, we propose analyzing the relationship between applied stress and the experimentally determined R/L values, which enables a more comprehensive understanding of the stressinduced orientation dynamics. During the fiber spinning process, the axial stress exerted on the fiber is proportional to the extension rate,[37,38] which can be expressed as the gradient of the fiber axial velocity:

$$\frac{dv\left(x\right)}{dx} = -\frac{2Q}{\pi} \cdot \frac{1}{R(x)^{3}} \cdot \frac{dR\left(x\right)}{dx} \tag{2}$$

where Q is the volumetric flow velocity. A positive (negative) extension rate indicates that there is tensile (compressive) stress applied on the fiber axial direction. To calculate the extension rate, we first derived the axial radius gradient d(R/R_{spin})/dx of different fibers from x = 0 to 1000 µm, and found that it has a linear correlation with the axial R/L gradient d(R/L)/dx (Figure 3d,e; Figure S21 and Note S5, Supporting Information). This result indicates that the $[d(R/L)/dx]/R^3$ may also correlate with the extension rate with a linear dependence. The extension rate is then calculated from dR/dx using Equation (2), and plotted with $[d(R/L)/dx]/R^3$ in Figure 3f. Indeed, [d(R/L)/dx]/R3 and extension rate show a negative linear correlation with:

$$\frac{d(R/L)}{dx} \cdot \frac{1}{R^3} = -5.3 \text{ (s mm}^{-4}) \cdot \frac{dv}{dx}$$
(3)

where dv/dx > 0 (< 0) corresponds to the extension (expansion) flow region. The above correlation indicates that a larger absolute value of extension rate will always result in greater R/L variation, and the fiber free from external force (dv/dx = 0) will retain its orientation structures. From the orientation controlling point of view, Equation (3) show that a negative extension rate induced by the flow interfacial self-adaption will lead to a positive R/L gradient in x-direction and a larger R/L value in fiber equilibrium state (Figure S1c, Supporting Information); while a positive extension rate from mechanical drawing will have an opposite influence (Figure S1e, Supporting Information). The nanomaterial orientation fine-tuning mechanism revealed by Equations (1) and (3) is theoretically universal, which can benefit the quantitative flow behavior analysis and orientation structure design of other nanomaterial fibers as well.

2.3. MA Performance and Orientation-Property Relationship in **Fibers**

Having elucidated the orientation structures of the fibers, we subsequently evaluated the MA properties and their dependence on orientation. To enhance the dielectric loss capability, GO/Alg aerogel fibers were thermally reduced into reduced graphene oxide/alginate (rGO/Alg) fibers (see Experimental Section). These fibers were cut into 5 mm segments and embedded into paraffin to fabricate coaxial ring samples for electromagnetic testing (see Experimental Section and Figure \$22a, Supporting Information). Cross-sectional SEM imaging confirmed that the internal orientation structures were well preserved in the paraffin matrix (Figure \$23, Supporting Information).

To standardize the nomenclature, the R/L value for parallel fibers (Figure 2d,h,l) was defined as zero, as justified by Equation (2). The electromagnetic parameters of rGO/Alg fibers with different R/L values were measured in the 2-18 GHz range using a coaxial transmission line method (Figure 4a,b). Both the real and imaginary parts of the permittivity decreased monotonically with increasing R/L, indicating that the dielectric properties are modulated by the internal orientation structures.

Based on these electromagnetic parameters, the reflection loss of each fiber was calculated (see Experimental Section and Figure S24, Supporting Information). Figure 4c presents the RL curves with minimum reflection loss (RLmin) and maximum EAB for each sample. Notably, both RL_{\min} and maximum EAB display a monotonic dependence on R/L (Figure 4d). The fiber with R/L =1.7 exhibited the best MA performance, with RL_{min} of -66.7 dB at 2.2 mm thickness and the maximum EAB of 6.28 GHz at 2.5 mm thickness. This performance surpasses most reported carbon-based powders, aerogels, and fibers at a moderate filler content (4 wt%) (Figure 4e; Table S2, Supporting Information).

To further explore the mechanism underlying this orientationdependent MA behavior, we first examined the impedance matching condition, which determines the ease with which electromagnetic waves can enter the material. A material exhibits good matching when the ratio between input impedance and free-space impedance ($|Z_{\rm in}/Z_0|$) is between 0.8 and 1.2. The calculated $|Z_{in}/Z_0|$ values (see Experimental Section and Figure \$25, Supporting Information) reveal that impedance matching improves with increasing R/L, consistent with the observed enhancement in MA performance (Figure 4d,f). Further analysis of the real and imaginary parts of impedance supports

16163028, 0, Downloaded from https

inelibrary.wiley.com/doi/10.1002/adfm.202519036 by Peking University Health, Wiley Online Library on [23/10/2025]. See the Terms

conditions) on Wiley Online Library for rules of use; OA articles are governed by the applicable Creative Commons I

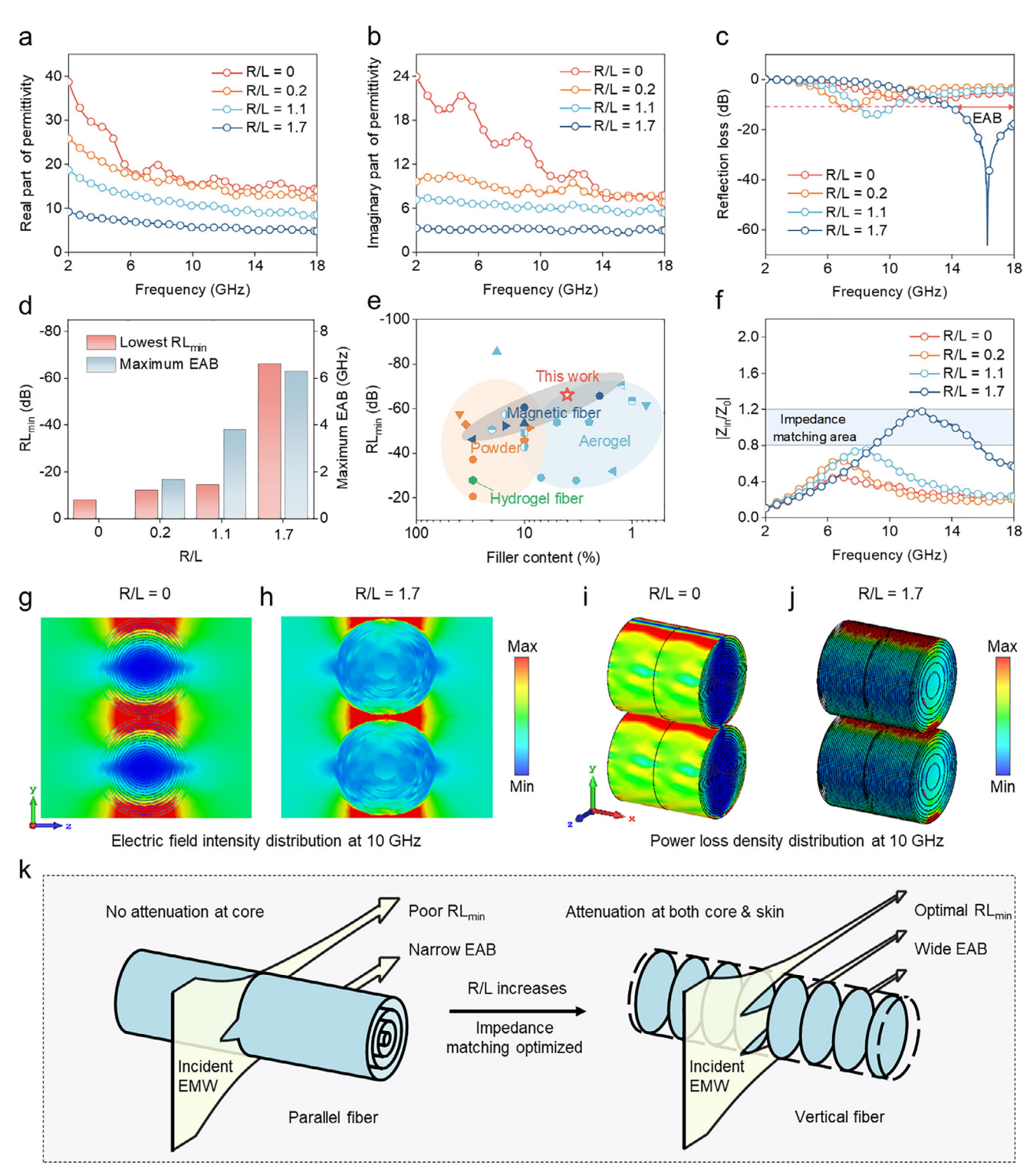


Figure 4. Orientation-dependent microwave attenuation performance of rGO/Alg fibers and the underlying mechanisms. a, b) Real (a) and imaginary (b) part of permittivity for rGO/Alg fibers with varying R/L values, measured over the 2–18 GHz range. c) Reflection loss curves showing the RL_{min} and maximum EAB values for different fibers. d) Summary of the RL_{min} and maximum EAB values as a function of R/L values. e) Comparison of the RL_{min} and filler content between the rGO/Alg fiber with R/L = 1.7 in this work and previously reported nanocarbon-based powders, aerogels, and fibers (see details in Table S2, Supporting Information). f) $|Z_{in}/Z_0|$ values indicating impedance matching performance for different samples at 2.5 mm thickness. g, h) Simulated electric field intensity distributions for fibers with low (g) and high (h) R/L values at 10 GHz. i, j) Corresponding power loss density distributions for fibers with low (i) and high (j) R/L values. k) Schematic illustration of the orientation-dependent microwave attenuation mechanism. Increased R/L enables deeper EM wave penetration and stronger power loss within the fiber core, thereby enhancing attenuation efficiency.

www.afm-journal.de

16163028.0, Downloaded from https://advanced.onlinelibrary.wiley.com/doi/10.1002/affm.202519036 by Peking University Health, Wiley Online Library on [23/10/2025]. See the Terms and Conditions (https://onlinelibrary.wiley.com/erms-and-conditions) on Wiley Online Library for rules of use; 0A articles are governed by the applicable Creative Commons Is

this trend (see Figure S26, Supporting Information). Additionally, the RL_{min} vs thickness profile for the fiber (R/L = 1.7) aligns well with the quarter-wavelength matching theory (Figure S27, Supporting Information). This result demonstrates that there is destructive interference between the incident wave at the fiber-air interface and the reflected wave within the material, which can further optimize the impedance matching condition.

We then derived the attenuation coefficient for the fibers to assess their intrinsic microwave attenuation ability (Figure \$28, Supporting Information). Interestingly, the fiber with R/L = 0 exhibited the highest attenuation coefficient, which decreased with increasing R/L. This is opposite to the trend in MA performance (Figure 4d). These results suggest that the attenuation coefficient is not the dominant factor determining MA performance (RL_{min} and maximum EAB); rather, impedance matching plays a crucial role. The superior performance of the R/L = 1.7 fiber, despite its lower attenuation coefficient, further reinforces this conclusion.

To identify the origin of the impedance matching difference, we ruled out several factors. Thermogravimetric analysis confirmed that all fibers had similar rGO-to-Alg mass ratios, excluding the absorber loading as a variable (Figures \$29 and \$30, Supporting Information). Raman spectroscopy, X-ray photoelectron spectroscopy (XPS), and elemental analysis showed minimal differences in defect density, chemical composition, or bonding state (Figures \$31-\$34, Supporting Information), aligning with the similarity in electrical conductivity (Figure \$35, Supporting Information). These results indicate that molecular-scale properties are not responsible for the observed impedance matching differences.

To better understand how orientation affects impedance matching, we performed electromagnetic simulations of electric field intensity and power loss distribution for fiber arrays under 10 GHz electromagnetic wave irradiation (see Experimental Section and Figure S36, Supporting Information). At low R/L, the electric field was confined to the skin region, with minimal penetration into the core (Figure 4g; Figure \$37a, Supporting Information). Consequently, energy dissipation occurred mainly at the periphery (Figure 4i; Figure \$37c, Supporting Information, and left panel of Figure 4k). In contrast, fibers with high R/L values allowed deeper electric field penetration into the core (Figure 4h; Figure S37c, Supporting Information), leading to more uniform and enhanced electromagnetic wave dissipation throughout the fiber cross-section (Figure 4j; Figure S37d, Supporting Information, and right panel of Figure 4k). Simulations at 18 GHz showed similar results, indicating the universality of this mechanism (Figure \$38, Supporting Information). In summary, orientation structure modifies internal electric field distribution, which directly impacts impedance matching and ultimately governs the MA performance of rGO/Alg fibers. The complete R/L-dependent MA mechanism is summarized in Figure 4k. We also crushed fibers with different R/L into powders and repeated the electromagnetic tests to verify the importance of orientation. The R/L-dependent trends in MA performance and impedance matching disappeared after powderization (Figures \$39-\$43, Supporting Information), providing direct evidence that orientation structure governs the observed behavior.

3. Conclusion

In summary, we established a comprehensive orientation finetuning strategy and a quantitative operando characterization system, enabling the fabrication and structural analysis of graphenebased fibers with tunable orientation distributions. A semiellipsoid shell model was developed to unify the orientation descriptions across fibers ranging from parallel to vertically aligned structures. This model also facilitated a quantitative understanding of the flow-mediated orientation control mechanism during wet spinning. The resulting fibers exhibited clear orientationdependent MA performance, with optimized EAB and RLmin values reaching 6.28 GHz and -66.7 dB, respectively. Electromagnetic simulations further revealed that graphene orientation significantly influences the internal electric field distribution. In particular, vertically aligned fibers more effectively attenuate electromagnetic waves polarized perpendicular to the fiber axis. Our orientation fine-tuning and operando characterization approaches provide promising tools for the development of next-generation orientation-engineered functional fibers.

4. Experimental Section

Materials: Graphene oxide aqueous solution (GO-3, single layer, lateral size = 40-50 µm, oxygen content = 30%-40%, Hangzhou Gaoxi Technology Co., Ltd.), sodium alginate (Energy Chemical), and calcium chloride (99.90%, Harveybio) were used as received without further purifica-

Preparation of GO/Alg and rGO/Alg Fibers: First, 20 g of 2 wt.% GO aqueous dispersion was diluted in 20 mL of deionized water, while 0.6 g of sodium alginate was dissolved in 30 mL of deionized water. Each solution was then homogenized with a planetary centrifugal mixer (Junzhi Speed-Mixer) at 3000 rpm for 5 min. Subsequently, coaxial wet spinning was performed using a coaxial needle (inner needle: inner diameter = 250 µm, outer diameter = 510 μ m; outer needle: inner diameter = 840 μ m, outer diameter = 1270 µm), where the 1 wt.% GO aqueous solution was used as the core fluid, and 2 wt.% sodium alginate aqueous solution was used as the shell fluid, and 3 wt.% CaCl₂ solution was chosen as the coagulation bath. The initial flow speeds of GO and Alg were 90.76 and 12.17 mm s^{-1} , respectively. By adjusting the drawing speed during wet spinning, GO/Alg hydrogel fibers with different R/L values were obtained. These hydrogel fibers were then pre-cooled in liquid nitrogen for 1 h and subsequently freeze-dried for 24 h to obtain GO/Alg aerogel fibers. The GO/Alg aerogel fibers were further annealed at 800 °C under argon atmosphere for 1 h to yield rGO/Alg fibers.

Simultaneous Polarimetry: The basic optical setups and working principles of simultaneous polarimetry can be found in Figure 1, Figure S2, and Note S1 (Supporting Information). Specifically, the whole system was mainly composed of an inverted microscope (Nikon ECLIPSE Ti-U), a QuadImage image splitter (Airy Technologies Co., Ltd, China), and a high-speed camera (pco.dimax cs3). A 550 nm bandpass filter (Thorlabs FBH550-10) was placed between the light source and sample to ensure monochromatic illumination. When taking the polarization images, all fibers were placed in transparent isotropic glass containers and immersed in water or a CaCl₂ aqueous solution to eliminate unwanted light scattering due to refractive index mismatches between fiber and environment. A ×4 objective was used in all measurements in this work. Before the measurement, the optical system was calibrated following the procedure described in the TXT file named "read_me" in Code \$1 (Supporting Information). For operando characterization, each frame of polarization images captured by a high-speed camera was put into the algorithm in Code S1 (Supporting Information) to calculate the orientation, average transmittance, and diattenuation distribution images after the operando characterization experiment. For longtime measurement, the optical system was calibrated every 1 h to ensure

www.afm-journal.de

16163028, 0, Downloaded from https://advanced.onlinelibrary.wiley.com/doi/10.1002/adfm.202519036 by Peking University Health, Wiley Online Library on [23/10/2025]. See the Terms and Conditions (https://onlinelibrary.wiley

com/terms-and-conditions) on Wiley Online Library for rules of use; OA articles are governed by the applicable Creative Commons I

the long-term measurement stability. The θ , $T_{ave.}$ and D distribution images of each frame were edited into a video using ImageJ. The final videos are shown in Videos \$1-s5 (Supporting Information). The frame rate of the high-speed camera was 100 fps.

Other Characterization Methods: The morphological structure of the fibers was characterized using SEM (Regulus8220, HITACHI, Japan) and focused-ion-beam SEM (Solaris, TESCAN, Czech Republic). The molecular-scale structures and chemical states of fibers were analyzed by X-ray photoelectron spectroscopy (AXI5 Supra, Kratos Analytical, UK) and Raman spectroscopy (laser wavelength = 532 nm, LabRAM Odyssey, Horiba, France). The electrical conductivity of the powders was measured using a Dual-Mode Four-Point Probe Tester (RTS-9, 4 Probes Tech, China). The rGO content in the fibers was determined via thermogravimetric analysis (Q600 SDT, TA, US).

Electromagnetic Parameters Measurement and MA Performance Analysis: The electromagnetic parameters of rGO/Alg fibers were tested by the coaxial transmission line method. The fibers were first chopped into 5 mmlength short-cut fibers. Following the fiber arrangement shown in Figure S22 (Supporting Information), 2.8 mg of short-cut fibers were then placed in a coaxial ring mold, and 67.2 mg of molten paraffin was uniformly injected into the mold. After cooling to room temperature, the paraffin ring was detached from the mold for the following measurement. A vector network analyzer (3656D, Ceyear, China) was used to test the electromagnetic parameters of different fibers in the range of 2–18 GHz, and the reflection loss of the samples was calculated according to the electromagnetic wave transmission line theory with the following equations:

$$RL(dB) = 20 \lg \left| \frac{Z_{in} - Z_0}{Z_{in} + Z_0} \right|$$
 (4)

$$Z_{in} = \sqrt{\frac{\mu_r}{\varepsilon_r}} \cdot Z_0 \cdot \tanh\left(i \cdot \frac{2\pi}{c} \cdot f \cdot d \cdot \sqrt{\mu_r \varepsilon_r}\right) \tag{5}$$

where μ_r and ϵ_r are the material complex permeability and permittivity, respectively, $Z_0=377\;\Omega$ is the free-space impedance, Z_{in} is the material input impedance, d is the paraffin ring thickness, f is the frequency, and c is the speed of light in vacuum.

Electromagnetic Simulation: CST STUDIO SUITE 2019 software was used to simulate the MA performance of fibers with different R/L values. The cross-sections of geometric models for different fibers are shown in Figure 2i-l. To exclude the influence of fiber radius and the thickness of semi-ellipsoid shells, all fibers in the simulation were set to have the same radius of $R = 250 \,\mu m$ and semi-ellipsoid shell thickness of R/1000. According to cross-section SEM images in Figure 2e-h, the distances between adjacent semi-ellipsoid shells were set to R/25 for R/L = 1.7 fiber, R/10 for R/L = 1.1 fiber, R/5 for R/L = 0.2 fiber, and R/20 for R/L = 0 fiber, respectively. The electromagnetic parameters of semi-ellipsoid shells were set to the same as those of graphite in the CST material library except for the electric conductivity, which was set as 1.25 S cm⁻¹ based on the experimental measurement (Figure S35, Supporting Information). The background was set as a vacuum for simplicity. In order to reduce the computational cost, the periodic unit cell boundaries in x- and y-directions were used, while open boundaries were set in z-direction (Figure S36, Supporting Information). A unit cell was composed of a fiber with a length of R/2. Lower and upper Y distances of background were set as R/100, considering the thickness of the insulating Alg shell (Figure S44, Supporting Information). The incident direction of linearly polarized plane EMW was set as from the positive z-direction to the negative z-direction. Based on the analysis of fiber geometry in the coaxial waveguide measurement, the electric field direction of the plane EMW was set as the y-direction (Figure S22, Supporting Information). The electric field intensity distribution and power loss density distribution of fibers were computed using a frequency domain solver.

Supporting Information

Supporting Information is available from the Wiley Online Library or from the author.

Acknowledgements

This work was financially supported by the Ministry of Science and Technology of China (2022YFA1203302 and 2022YFA1203304), the National Natural Science Foundation of China (Grant Nos. T2188101, 52021006, 52302034, 22494642, and 22494641), the Strategic Priority Research Program of CAS (XDB36030100), the Beijing National Laboratory for Molecular Sciences (BNLMS-CXTD-202001) and the Shenzhen Science and Technology Innovation Commission (KQTD20221101115627004).

Conflict of Interest

The authors declare no conflict of interest.

Author Contributions

H.H. and Z.W. contributed equally to this work. H.H., L.T., and X.G. conceived the project ideas and designed the experiments. H.H. built the simultaneous polarimetry, designed the corresponding MATLAB algorithm, and performed the electromagnetic simulation. Z.W. and T. L. carried out the synthesis and characterization of different fibers. All authors contributed to the interpretation of experimental and simulation results and co-wrote the manuscript. L.T., X.G., and J.Z. supervised this project.

Data Availability Statement

The data that support the plots within this paper and other findings of this study are available from the corresponding authors upon reasonable request.

Keywords

coaxial wet-spinning, graphene fiber, microwave absorption, nanomaterial orientation, simultaneous polarimetry

> Received: July 23, 2025 Revised: September 14, 2025 Published online:

- [1] M. S. Cao, X. X. Wang, M. Zhang, W. Q. Cao, X. Y. Fang, J. Yuan, Adv. Mater. 2020, 32, 1907156.
- [2] B. Wen, M. S. Cao, M. M. Lu, W. Q. Cao, H. L. Shi, J. Liu, X. X. Wang, H. B. Jin, X. Y. Fang, W. Z. Wang, J. Yuan, Adv. Mater. 2014, 26, 3484.
- [3] M. S. Cao, X. X. Wang, W. Q. Cao, X. Y. Fang, B. Wen, J. Yuan, Small 2018, 14, 1800987.
- [4] B. Wen, M. S. Cao, Z. L. Hou, W. L. Song, L. Zhang, M. M. Lu, H. B. Jin, X. Y. Fang, W. Z. Wang, J. Yuan, Carbon 2013, 65, 124.
- [5] Y. X. Xia, W. W. Gao, C. Gao, Adv. Funct. Mater. 2022, 32, 2204591.
- [6] M. S. Cao, C. Han, X. X. Wang, M. Zhang, Y. L. Zhang, J. C. Shu, H. J. Yang, X. Y. Fang, J. Yuan, J. Mater. Chem. C 2018, 6, 4586.
- [7] Y. L. Hou, Z. Z. Sheng, C. Fu, J. Kong, X. T. Zhang, Nat. Commun. 2022, 13, 1227.
- [8] S. P. Wang, Q. C. Liu, S. K. Li, F. Z. Huang, H. Zhang, ACS Nano 2024, 18, 5040
- [9] Z. C. Wu, K. Pei, L. S. Xing, X. F. Yu, W. B. You, R. C. Che, Adv. Funct. Mater. 2019, 29, 1901448.
- [10] X. H. Wang, J. Qin, J. Cui, L. Huang, Y. Yuan, Y. B. Li, Adv. Fiber Mater. 2022. 4. 1164.
- [11] M. L. Yang, Y. Yuan, Y. Li, X. X. Sun, S. S. Wang, L. Liang, Y. H. Ning, J. J. Li, W. L. Yin, R. C. Che, Y. B. Li, Carbon 2020, 161, 517.

ADVANCED
FUNCTIONAL
MATERIALS

16163028, 0, Downloaded

onlinelibrary.wiley.com/doi/10.1002/adfm.202519036 by Peking University Health, Wiley Online Library on [23/10/2025]. See the Terms

conditions) on Wiley Online Library for rules of use; OA articles are governed by the applicable Creative Commons I

- [12] L. Li, H. T. Zhao, P. B. Li, L. Z. Meng, J. P. Yang, J. T. Bai, G. Wang, J. F. Yan, Compos. Part. B-Eng. 2022, 243, 110121.
- [13] X. H. Wu, G. Hong, X. T. Zhang, Langmuir 2019, 35, 3814.
- [14] S. K. Singh, M. J. Akhtar, K. K. Kar, ACS Appl. Mater. Interfaces 2018, 10, 24816.
- [15] R. Zhao, B. Q. Liang, Y. Shia, Q. Dong, T. X. Li, J. W. Gu, Y. Ma, J. Zhang, S. Melhi, A. S. Alshammari, Z. M. El-Bahy, Z. H. Guo, *Carbon* 2024, 229, 119513.
- [16] H. G. Liu, Y. J. Yang, N. Tian, C. Y. You, Y. Yang, Carbon 2024, 217, 118608.
- [17] W. Q. Cao, X. X. Wang, J. Yuan, W. Z. Wang, M. S. Cao, J. Mater. Chem. C 2015, 3, 10017.
- [18] X. Y. Fang, X. X. Yu, H. M. Zheng, H. B. Jin, L. Wang, M. S. Cao, Phys. Lett. A 2015, 379, 2245.
- [19] L. Y. Liang, Q. M. Li, X. Yan, Y. Z. Feng, Y. M. Wang, H. B. Zhang, X. P. Zhou, C. T. Liu, C. Y. Shen, X. L. Xie, ACS Nano 2021, 15, 6622.
- [20] C. Yu, B. L. Xie, X. H. Yao, N. Hu, J. H. Guo, X. H. Jiang, A. T. Smith, L. Y. Sun, *Matter* 2023, 6, 4321.
- [21] Y. C. Zhang, R. Ding, P. G. Su, F. R. Zeng, X. X. Jia, Z. Y. Hu, Y. Z. Wang, H. B. Zhao, Adv. Funct. Mater. 2025, 35, 2414683.
- [22] X. S. Zhang, X. D. Lei, X. Z. Jia, T. Z. Sun, J. J. Luo, S. C. Xu, L. J. Li, D. Yan, Y. L. Shao, Z. Z. Yong, Y. Y. Zhang, X. Q. Wu, E. L. Gao, M. Q. Jian, J. Zhang, *Science* 2024, 384, 1318.
- [23] P. Li, Z. Q. Wang, Y. X. Qi, G. F. Cai, Y. J. Zhao, X. Ming, Z. Z. Lin, W. G. Ma, J. H. Lin, H. Li, K. Shen, Y. J. Liu, Z. Xu, Z. P. Xu, C. Gao, Nat. Commun. 2024, 15, 409.
- [24] Y. Wang, S. J. Wang, Y. Gao, P. Li, B. Zhao, S. P. Liu, J. Y. Ma, L. D. Wang, Q. C. Yin, Z. Q. Wang, L. Peng, X. Ming, M. Cao, Y. J. Liu, C. Gao, Z. P. Xu, Z. Xu, Sci. Adv. 2024, 10, adm7737.
- [25] X. Ming, A. R. Wei, Y. J. Liu, L. Peng, P. Li, J. Q. Wang, S. P. Liu, W. Z. Fang, Z. Q. Wang, H. Q. Peng, J. H. Lin, H. G. Huang, Z. P. Han, S.

- Y. Luo, M. Cao, B. Wang, Z. Liu, F. L. Guo, Z. Xu, C. Gao, Adv. Mater. **2022**. 34. 2201867.
- [26] F. Wang, W. Z. Fang, X. Ming, Y. J. Liu, Z. Xu, C. Gao, Appl. Phys. Rev. 2023, 10, 011311.
- [27] H. Shi, B. Wang, L. D. Wang, P. J. Zhang, X. Ming, Y. Y. Hao, J. H. Lu, Y. Gao, W. W. Gao, H. Y. Sun, P. Li, Z. Xu, Y. J. Liu, C. Gao, *Carbon* 2024, 221, 118947.
- [28] G. Q. Xin, W. G. Zhu, Y. X. Deng, J. Cheng, L. T. Zhang, A. J. Chung, S. De, J. Lian, Nat. Nanotechnol. 2019, 14, 168.
- [29] D. Kiriya, R. Kawano, H. Onoe, S. Takeuchi, Angew. Chem. Int. Ed. 2012, 51, 7942.
- [30] M. Trebbin, D. Steinhauser, J. Perlich, A. Buffet, S. V. Roth, W. Zimmermann, J. Thiele, S. Förster, Proc. Natl. Acad. Sci. U.S.A. 2013, 110, 6706.
- [31] H. Park, K. H. Lee, Y. B. Kim, S. B. Ambade, S. H. Noh, W. Eom, J. Y. Hwang, W. J. Lee, J. Huang, T. H. Han, Sci. Adv. 2018, 4, aau2104.
- [32] H. Y. Niu, H. C. Guo, L. Kang, L. C. Ren, R. C. Lv, S. L. Bai, Nano-Micro Lett. 2022, 14, 153.
- [33] X. L. Zhu, Y. Zhang, Z. M. Man, W. Y. Lu, W. Chen, J. H. Xu, N. Z. Bao, W. X. Chen, G. Wu, Adv. Mater. 2023, 35, 2307186.
- [34] X. L. Zhu, H. Qiu, Y. Zhang, Z. M. Man, W. Y. Lu, N. Z. Bao, G. Wu, Adv. Fiber Mater. 2024, 6, 312.
- [35] J. S. Fu, Y. C. Li, T. Z. Zhou, S. L. Fang, M. M. Zhang, Y. L. Wang, K. Li, W. W. Lian, L. Wei, R. H. Baughman, Q. F. Cheng, Sci. Adv. 2025, 11, adt1560.
- [36] G. X. Zhao, T. L. Wu, R. H. Wang, Z. Li, Q. Z. Yang, L. Wang, H. W. Zhou, B. R. Jin, H. Liu, Y. S. Fang, D. Wang, F. Xu, Sci. Adv. 2023, 9, adj5407.
- [37] C. D. Han, L. Segal, J. Appl. Polym. Sci. 1970, 14, 2973.
- [38] C. D. Han, L. Segal, J. Appl. Polym. Sci. 1970, 14, 2999.